Publications of the Astronomical Society of Australia (2025), **42**, e137, 17 pages
doi:10.1017/pasa.2025.10094

CAMBRIDGE UNIVERSITY PRESS

Research Article

GaLactic and extragalactic all-sky Murchison Widefield Array survey eXtended (GLEAM-X) III: Galactic plane

Silvia Mantovanini[1], Natasha Hurley-Walker[1], Kathryn Ross[2,1], Stefan Duchesne[3], Gemma Anderson[1] and Timothy James Galvin[3]

[1]International Centre for Radio Astronomy Research, Curtin University, Bentley, WA, Australia, [2]Australian SKA Regional Centre (AusSRC), Curtin University, Bentley, WA, Australia and [3]CSIRO Space and Astronomy, Bentley, WA, Australia

Abstract

We present the third data release for the Galactic and Extragalactic All-Sky Murchison Widefield Array eXtended (GLEAM-X) survey, covering $\approx 3\,800$ deg^2 of the southern Galactic Plane (GP) with $233° < l < 44°$ and $|b| < 11°$ across a frequency range of 72–231 MHz divided into 20 sub-bands. GLEAM-X observations were taken using the 'extended' Phase-II configuration of the Murchison Widefield Array (MWA), which features baselines ranging from approximately 12 m to 5 km. This configuration limits sensitivity to the diffuse structure of the GP, with an angular resolution range of about $45''$ to $2'$. To achieve lower noise levels while being sensitive to a wide range of spatial scales ($45'' - 15°$), we combined these observations with the previous Galactic and Extragalactic All-Sky Murchison Widefield Array (GLEAM) survey. For the area covered, we provide images spanning the whole frequency range. A wide-band image over 170–231 MHz, with RMS noise of $\approx$ 3–6 mJy beam^{-1} and source position accuracy within 1 arcsec, is then used to perform source-finding, which yields 98 207 elements measured across 20 × 7.68 MHz frequency bands. The catalogue is 90% complete at 50 mJy within $233° < l < 324°$ and at 125 mJy in $290° < l < 44°$, while it is 99.3% reliable overall. All the images and the catalogue are available online for download.

Keywords: techniques: interferometric; surveys

(Received 6 May 2025; revised 1 September 2025; accepted 1 September 2025)

1. Introduction

Radio astronomy surveys along the Galactic Plane (GP) have undergone significant upgrades over the last century, advancing our understanding of the Milky Way thanks to sky coverage, sensitivity, and resolution improvements. GP surveys are essential in understanding the complex structure of the Milky Way, its composition, how it evolves and what emission processes come into place. Spectral index studies are key to differentiating the emission mechanisms occurring in various objects (Cavallaro et al. 2017) and understanding how they evolve and interact. Mid-to-high radio frequency bands can provide insights into the thermal emission of star-forming regions (Brunthaler et al. 2021). In contrast, low radio frequencies are particularly useful for negative spectrum sources (assumed to be $S \propto \nu^{\alpha}$ with α having negative values), such as pulsars (Swainston et al. 2021), or to analyse free-free absorption and synchrotron self-absorption traces along the plane, useful in constraining the distribution of Cosmic Ray (CR) electrons and Galactic Magnetic Field (GMF) (Su et al. 2018; Nord et al. 2006). Moreover, supernova remnants (SNRs) offer key insights into the life cycle and evolution of stars in our Galaxy (Dubner & Giacani 2015).

Corresponding author: Silvia Mantovanini; Email: silvia.mantovanini@postgrad.curtin.edu.au.

Cite this article: Mantovanini S, Hurley-Walker N, Ross K, Duchesne S, Anderson G and Galvin TJ. (2025) GaLactic and extragalactic all-sky Murchison Widefield Array survey eXtended (GLEAM-X) III: Galactic plane. *Publications of the Astronomical Society of Australia* **42**, e137, 1–17. https://doi.org/10.1017/pasa.2025.10094

Mid-frequency surveys, such as the ongoing Evolutionary Map of the Universe (EMU; Norris et al. 2021) at 944 MHz using the Australian Square Kilometre Array Pathfinder (ASKAP; Hotan et al. 2021) telescope, and the new SARAO[a] MeerKAT Galactic Plane Survey (SMGPS; Goedhart et al. 2024) at 1 300 MHz, demonstrate the impressive results of surveys with modern wide-band mid-frequency receivers in terms of resolution and sensitivities, obtaining a few arcseconds and 10–20 μJy beam^{-1}, respectively (Anderson et al. 2025).

Despite the notable success of the latest surveys, we still face certain limitations. While these surveys often aim for full sky coverage, the small field of view at high frequencies (GHz regime) makes the data acquisition process less efficient, requiring more observing time to cover large areas. Another limitation is the maximum angular scale that mid-radio surveys are sensitive to, which is intrinsically tied to the size of the interferometer dishes and their array configuration, which limits the baseline coverage for the largest spatial scales. Goedhart et al. (2024) analysed the problem for the SMGPS in detail, highlighting that the spectra for sources with a radius greater than $2'$ can be significantly inaccurate and should not be used. The MeerKAT frequency-dependent sensitivity recovers a higher fraction of the flux densities for extended sources at the lowest frequency. The result is an apparent steepening in the spectral index for non-point-like sources. Although the Parkes Galactic All-Sky Survey (PEGASUS) project showed the

[a]South African Radio Astronomy Observatory.

© The Author(s), 2025. Published by Cambridge University Press on behalf of Astronomical Society of Australia. This is an Open Access article, distributed under the terms of the Creative Commons Attribution licence (https://creativecommons.org/licenses/by/4.0/), which permits unrestricted re-use, distribution and reproduction, provided the original article is properly cited.

first results of addressing this limitation by providing images sensitive to larger scales, which can be combined with EMU data to produce more accurate sky images, this project is still ongoing and will require time to be completed. As a result, neither of these surveys is sensitive to a broad range of spatial scales crucial for science cases, such as detecting and performing spectral analysis of diffuse structures within the Galaxy, like star-forming regions (Medina et al. 2024), supernova remnants and Galactic bubbles (Ingallinera et al. 2014).

On the other hand, low-frequency surveys provide critical insights into the non-thermal sky. A key strength is offered by low-frequency interferometers, such as the established Giant Metrewave Radio Telescope (GMRT Swarup et al. 1991), which offers moderate angular resolution with sensitivity to both compact and moderately extended emission (up to $\approx 1^\circ$ at 150 MHz), and latest instruments such as the LOw Frequency ARray (LOFAR) and the Murchison Widefield Array (MWA, Tingay et al. 2013; Wayth et al. 2018), which employ dense core configurations with predominantly short baselines to enhance sensitivity to large angular scales. This feature allows low-frequency surveys to recover extended emission from diffuse structures, such as SNRs and HII regions (Castelletti et al. 2007), far more effectively than higher-frequency surveys like EMU or SMGPS.

However, it is worth mentioning that ionospheric effects become increasingly problematic at these lower frequencies, introducing strong, frequency-dependent phase distortions ($\propto \nu^{-2}$) that vary across the field of view. These distortions can lead to position shifts and smearing of sources in the images if not properly corrected (Intema et al. 2009). The severity of these effects increases during periods of high ionospheric activity and toward lower elevations. LOFAR is actively implementing complex, direction-dependent calibration schemes to correct spatially varying ionospheric delays (van Weeren et al. 2016), essential for achieving accurate astrometry.

MWA, the low-frequency precursor of the SKAO, presents an extensive field-of-view (10^2–10^3 deg^2) and a wide frequency band 80–300 MHz, ideal for all-sky surveys south of declination (Dec) +30°. The instrument Phase I configuration (with a baseline range varying approximately from 7 m to 2.5 km – see Appendix 3) enabled the creation of the Galactic and Extragalactic All-sky MWA (GLEAM; Wayth et al. 2015) survey, which, thanks to the abundance of short baselines, has spatial scale sensitivity to ($2' - 15^\circ$) reaching noise levels of 10 mJy beam^{-1} in the extragalactic sky (Hurley-Walker et al. 2017) and 50–100 mJy beam^{-1} along the GP (Hurley-Walker et al. 2019). GLEAM-GP enabled detailed studies of synchrotron emission, thermal absorption, and spectral turnovers, providing new insights into the structure and conditions of the interstellar medium. Its sensitivity to large-scale, diffuse emission has allowed the mapping of the GMF (Polderman, Haverkorn, & Jaffe 2020), investigations of cosmic ray propagation (Su et al. 2018), and the discovery of previously unidentified SNRs and HII regions (Hurley-Walker et al. 2019b; Anderson et al. 2017).

The 'extended' Phase II configuration of MWA (baseline range from ≈ 12 m to 5 km – see Appendix 3), on the other hand, used doubled length baselines to collect the data for the GLEAM-eXtended (GLEAM-X; Hurley-Walker et al. 2022; Ross et al. 2024) survey, which is incrementally being made available to the community as portions are completed. The longer baselines allow GLEAM-X to effectively capture smaller scales ($45'' - 20'$), and its lowered confusion limit enables better sensitivity over long integrations (~ 1 mJy beam^{-1}).

Here we present the GLEAM-X Galactic Plane survey (GLEAM-X-GP), which combines data from the GLEAM and GLEAM-X surveys, achieving a synergistic combination of resolution and sensitivity to an ample range of spatial scales across an observing band of 72–231 MHz. Several approaches have been developed to combine data from multiple surveys to address the problem of missing short spacings in interferometric imaging, e.g. feathering in the image plane (Cotton 2017). Some large-area surveys, such as the GLObal view on STAR formation in the Milky Way (GLOSTAR Brunthaler et al. 2021) and VLA Galactic Plane Survey (VGPS Stil et al. 2006), have implemented short-spacing corrections at multiple frequencies to improve the recovery of extended emission. In this work, we apply joint deconvolution to offer a consistent reconstruction of structures, avoiding accentuating deconvolution artefacts or calibration errors that might be present in individual image methodologies. In doing so, we will have multi-frequency sky coverage of the southern plane with sensitivity to a broad range of spatial scales, enabling accurate flux density measurements even for larger sources.

This paper presents the data reduction used to produce images covering the GLEAM-X-GP and an associated catalogue over the longitude range of $233^\circ < l < 44^\circ$ and within latitudes $|b| < 11^\circ$. Section 2 briefly summarises the observations. Section 3 describes the calibration, imaging and mosaicking procedures. Section 4 describes the derivation of a source catalogue along with a thorough assessment of its quality. Section 5 discusses the science applications that this release can achieve. Section 6 concludes with a short summary.

2. Observations

GLEAM and GLEAM-X observations were collected using similar strategies to efficiently cover the entire sky south of +30° in Dec. The observations were performed in drift-scan mode, in which the telescope pointing remained fixed while the sky drifted through the instrument's primary beam. For telescopes like the MWA, pointing refers to the electronically formed beams created by applying time delays or phase shifts to the signals from individual components to direct the telescope's sensitivity toward a desired region of the sky without moving the instrument. Seven pointings have been used at Decs centred on −72°, −55°, −40.5°, −26.7°, −13°, +1.6°, and +18.3°. The frequency range is divided into five bands 30.72 MHz wide: 72–103 MHz, 103–134 MHz, 139–170 MHz, 170–200 MHz, and 200–231 MHz, avoiding the band around 137 MHz due to contamination by the OrbComm satellite constellation. Each pointing was observed for approximately two minutes per band, iterating over the whole frequency range every 10 min. Observations were repeated over multiple nights; during each night, bright calibrator sources were observed repeatedly over the five frequency channels to obtain amplitude and phase gain solutions (listed by Hurley-Walker et al. 2017).

The 'extended' Phase II configuration of the MWA (described by Wayth et al. 2018) resulted in a smaller synthesised beam, which reduced the confusion limit in GLEAM-X from ≈ 2 mJy beam^{-1} to ≈ 0.3 mJy beam^{-1} at 200 MHz (Paterson et al. submitted). These advancements enabled longer integration times, allowing deeper observations and lower noise levels (Hurley-Walker et al. 2022). GLEAM observations were conducted over

https://doi.org/10.1017/pasa.2025.10094 Published online by Cambridge University Press

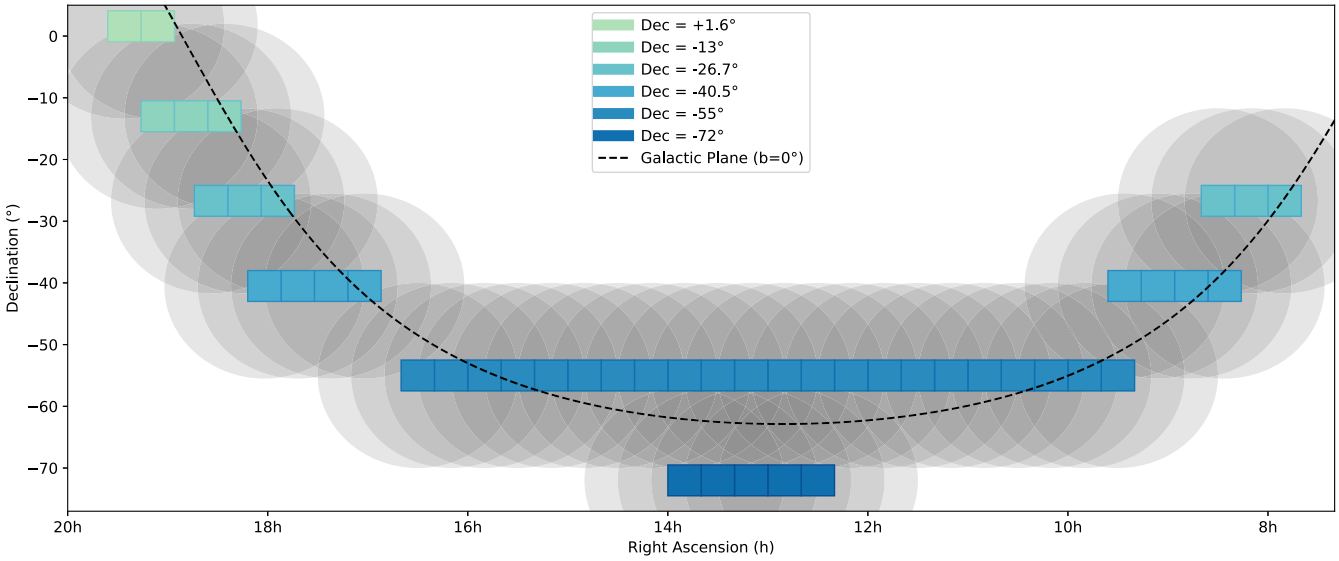


Figure 1. Representation of the grouping strategy for GLEAM and GLEAM-X. Each rectangle defines a group of 10–15 observations whose pointing centres fall within the coordinates of the boxed region, ensuring complete coverage over the GP across the declination range. Circular regions indicate individual fields of view, with overlaps between adjacent circles providing continuous coverage. The dashed black line marks the GP ($b = 0°$) in FK5 coordinates.

≈ 28 nights from August 2013 to June 2014, with additional observations in 2015 to re-observe regions where ionospheric conditions were particularly poor. GLEAM-X was observed over a three-year period from January 2018 to October 2020 for a total of 113 nights. Table D1 provides the first four lines of the table summarising all the observations used to create the final image of the GP. The full table can be downloaded from AAO Data Central.

3. Data reduction

GLEAM and GLEAM-X data have been jointly deconvolved, and all visibilities are used together to create one (dirty) image for deconvolution to achieve sensitivity to all the angular scales between $45'' - 15°$ while increasing the S/N of the sources. We employed the Image Domain Gridding (IDG; van der Tol, Veenboer, & Offringa 2018) algorithm implemented in WSClean (*w*-stacking clean; Offringa et al. 2014) for the data combination, efficiently converting extensive datasets from the visibility to the image domain. When combining data from multiple observations, IDG uses direction and time-dependent convolution kernels during the gridding stage to align the contributions from each observation onto a common grid. This approach ensures that direction-dependent (ionospheric) distortions are minimised. This is advantageous when compared to standard tools (e.g. TCLEAN in CASA CASA Team et al. 2022 and WSClean), which only apply these corrections in a post-imaging phase or do not support them at all. Furthermore, IDG enables a *hybrid* mode with Graphical Processing Units (GPUs) to perform the gridding and fast Fourier transforms, significantly decreasing the computational costs and making joint imaging feasible for large datasets.

We divided the GLEAM and GLEAM-X observations into small groups comprising approximately 10–15 observations, all with pointing centres with the same Dec and spanning a RA range of $\approx 5°$, as represented in Figure 1. While each group is ideally balanced to include data from both surveys to ensure adequate representation, this was not always feasible due to the quality constraints (see Sections 3.1–3.3) of the observations.

The data reduction performed in this work is heavily based on the GLEAM-X pipeline[b] described in full by Hurley-Walker et al. (2022), and summarised in the flowchart of Figure 2. Some improvements to data processing have been introduced to increase the image quality of the GP pointings and account for the presence of bright and extended radio sources that dominate the plane. Furthermore, we implemented additional steps to prepare the data to be jointly deconvolved and then mosaicked to form the final image. Here, we summarise the reduction steps, highlighting whether they have been changed from the previous methodology.

3.1 Calibration and flagging

We began assessing the quality of the observations covering the plane. We calibrated each 2-min observation via transferring amplitude and phase gains solutions obtained by the closest bright calibrator during the same night. An in-field calibration using the GLEAM sky model is executed if the calibrator observation gains are unavailable; for this purpose, we used all the baselines except the shortest (< 100 m) and longest (> 2.5 km) to, respectively, avoid contamination from diffuse emission, and to match the resolution of the GLEAM-based calibration sky model (described by Hurley-Walker et al. 2022). We visually inspected the solutions for every observation to assess the calibration quality; we discarded all observations with anomalies or unrealistic values of amplitude and phase gains over frequency.

To account for Radio Frequency Interference (RFI) contamination, we implemented an extra flagging stage for those observations in the lowest frequency channel (72–103 MHz), where more RFI is observed. Medians are calculated for Stokes I amplitudes of the visibilities for each measurement set using a window of 55

[b] https://github.com/GLEAM-X/GLEAM-X-pipeline.

https://doi.org/10.1017/pasa.2025.10094 Published online by Cambridge University Press

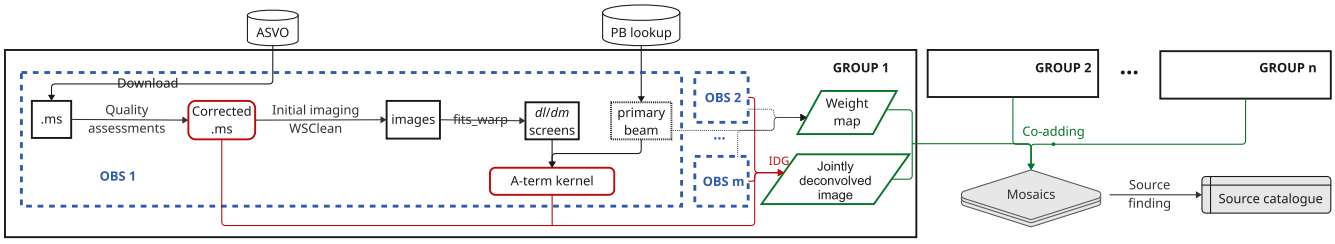


Figure 2. Flow diagram of the data reduction procedure. The diagram shows the main processing steps, from downloading the observations of each group to adding all the IDG group images to form the final mosaic.

channels at a time. Every channel with a median value greater than 0.5 σ – where σ is the standard deviation within the window – is flagged (removed). We additionally flagged two fine channels at the edges of each coarse channel (24, each 1.28 MHz wide) to avoid leakage. This ensures that only high-quality data is used for calibration and imaging.

Another origin of contamination is the presence of bright radio sources that fall in the sidelobes of our observation primary beam. We used the approach described by Ross et al. (2024) to deal with this issue. For each observation, we phase-rotate the visibilities using CHGCENTRE to match the coordinates of the source, then use WSCLEAN to form a shallow image 128 × 128 pixels in size to create a model of the object. Once the model is created, it is subtracted from the observation measurement set visibilities, which are then phase-rotated back to their original location. Every observation goes through this process, and all the bright sources above the horizon and falling in their sidelobes are subtracted. If the distance of the source from the pointing centre is $\leq 30°$, the process does not apply as the source will be properly cleaned during the imaging stage. Centaurus A is dealt with with a slightly different approach because of its high surface brightness and diffuse extension. For this reason, Centaurus A is subtracted from the visibilities even if it is on the edge of the observations. The subtraction is performed for observations with a pointing within $170° < RA < 250°$ to reduce the artefacts and the root-mean-square (RMS) noise level of the final image. In this case, the size of the shallow box is increased to 600 × 600 pixels to better model Centaurus A's large-scale emission.

3.2 Initial snapshot imaging

Initial 2-min images of each observation of the GP are generated by WSCLEAN using the settings described in the survey description papers (Hurley-Walker et al. 2019a and 2022 for GLEAM and GLEAM-X observations, respectively). We do not directly use these images for the final mosaic; they are utilised to assess the quality of the observation data by inspecting potential artefacts caused by residual RFI or bright sources and calibration performance. The detected position of the sources is saved as a reference point for ionospheric corrections, which is essential for enabling the joint deconvolution of each group of observations. These corrections ensure accurate source localisation, as described in Section 3.3. In the following, we will briefly list the parameters that vary between the two surveys and the parameters we have implemented in this work:

- **-SIZE**: GLEAM pixel images of 4 000 × 4 000 and 8 000 × 8 000 pixel images for GLEAM-X to encompass the field-of-view down to 10% of the primary beam and a frequency-dependent pixel scale to ensure each image has 3.5–5 pixels per FWHM of the restoring beam;
- **-WEIGHT**: different Briggs robust parameters (Briggs 1995) as a good compromise between resolution and sensitivity for the two configurations of the MWA: −1 (close to uniform weighting) is chosen for GLEAM to maximise the resolution and suppress the PSF sidelobes, while +0.5 is chosen for GLEAM-X to optimise the overall RMS noise – i.e. to improve sensitivity, which is ideal for detecting fainter signals;
- **-MULTISCALE-SCALE-BIAS**: increased the multiscale bias parameter (Offringa & Smirnov 2017) from the default value of 0.6 to 0.7 only for GLEAM-X observations to reduce the effects of diffuse emissions, which sometimes otherwise led to convergence problems or poorly cleaned point sources.

To avoid affecting the remaining observations of each group, we discarded the 2-min observations that show an exceptionally high RMS or residual artefacts we could not remove in the previous steps (see Section 3.1). Common problems are the presence of strikes across the image: vertical or horizontal are most likely caused by residual RFI; radial and originating from bright sources in the field caused by deconvolution errors; bright streaks radiating from outside the field of view caused by sources in the edges of the primary beam or the sidelobes; and regular striping around bright sources, or distortion of sources caused by poor calibration.

3.3 Astrometric calibration

To measure the position shifts induced by the ionosphere, we applied a similar methodology described in Hurley-Walker et al. (2019a) and later in Hurley-Walker et al. (2022). We used AEGEAN (Hancock et al. 2012; Hancock, Trott, & Hurley-Walker 2018) on each 2-min observation to determine the position of point sources in the image. We cross-matched it with a reference catalogue composed of a sparse (no internal matches within 3′) and unresolved (integrated to peak flux density ratio of <1.2) sample of the NRAO VLA Sky Survey (NVSS, Condon et al. 1998) at 1.4 GHz and the Sydney University Molonglo Sky Survey (SUMSS, Mauch et al. 2003) at 843 MHz respectively for the northern and southern sky. FITS WARP (Hurley-Walker & Hancock 2018) is ideal for accurately creating a model of the sources' pixel offsets by a cross-match between the snapshot and the reference catalogue. However, NVSS and SUMSS do not cover the sky area between $252° < l < 353°$ and $b < |11°|$; we selected the Rapid ASKAP Continuum Survey (RACS; McConnell et al. 2020; Hale

https://doi.org/10.1017/pasa.2025.10094 Published online by Cambridge University Press

et al. 2021) to fill in the gap in this region. For this purpose, we applied the criteria mentioned above to the RACS catalogue and selected a subset of only bright sources with integrated flux above 50 mJy at 888 MHz. We concatenated the catalogues, excluding internal matches of 3′. The position shifts along both axes in the sky plane (l and m) are saved into FITS-format cubes that will be applied to the final IDG image to correct for the ionospheric effects as will be described in Section 3.4.

We analysed the distribution of pipeline failures across the five 30 MHz bands. The results indicate lower frequencies (72–103 MHz) exhibit higher failure rates, particularly during the imaging stage, whereas higher frequencies (170–200 MHz) show fewer losses overall. Among the pipeline stages, calibration and post-imaging checks account for most failures, highlighting how these steps are critical data loss points in the pipeline. In appendix Appendix 1, we report the percentage of observations discarded due to high ionospheric activity as a function of time (see Figure A1). After assessing the quality of the observations, 57% were retained for the final imaging, while the remaining 43% were discarded due to quality issues. Of the successful observations, 53% came from GLEAM-X and 47% from GLEAM, reflecting the balanced contribution of both surveys to the final dataset.

3.4 Joint deconvolution

We now run the IDG algorithm implemented in WSCLEAN on GLEAM and GLEAM-X observation groups. The algorithm requires a configuration file characterising the direction-dependent effects we must account for in the cleaning process (the a-term corrections). The file points to the FITS cubes generated in Section 3.3 to correct the position of sources in the image by applying a position shift based on the previously saved information. During cleaning, we also correct for the MWA primary beam (Full Embedded Element model Sokolowski et al. 2017), an instrumental effect of the antennae, which are assumed to have identical responses over the whole array. Following the previous data releases (Hurley-Walker et al. 2017; Ross et al. 2024), the primary beams are calculated and interpolated as required using code developed by Morgan & Galvin (2021) for each element of the group. Finally, the beam correction is averaged across the full set of observations, improving the final image quality.

IDG also accounts for w-terms in wide-field imaging caused by the large field of view (can extend up to 30° depending on the frequency band) by incorporating w-corrections directly into the gridding process. Without these corrections, the standard two-dimensional Fourier transform of visibilities assumption (i.e., flat-sky approximation) becomes invalid, leading to artefacts around sources far from the phase centre, showing smearing. Ultimately, for each observation, we performed a visibilities phase rotation using CHGCENTRE to match the average pointing centre of all the observations in the group.

In the following, we list the parameters that vary compared to the 2-min observation WSCLEAN imaging run (presented in Section 3.2) and the parameters added to implement the new algorithm:

- **-AUTO-MASK**: initial masking threshold to control which regions are cleaned, set to 3, meaning only pixels with brightness above three times the estimated noise level are included during deconvolution. Cleaning will continue until the **-AUTO-THRESHOLD** stopping criterion of every major deconvolution iteration is reached. A threshold factor of 0.5 is chosen to reduce losses in flux densities for extended objects in the GP.
- **-SIZE**: pixel images of 8 000 × 8 000 and a frequency-dependent pixel scale (0.5/central frequency expressed in MHz) to ensure each image has 3.5–5 pixels per FWHM of the restoring beam;
- **-WEIGHT**: a Briggs robust parameter (Briggs 1995) of −0.25 as a good compromise between resolution and sensitivity for the two configurations of the MWA;
- **-IDG-MODE**: IDG is used in a hybrid mode using 1 NVIDIA Tesla V100 Tensor Core GPU per job, which increased processing efficiency.

3.5 Mosaicking

The same basic image quality checks applied in Section 3.3 are performed on each of the resulting 900 × 7.68 MHz IDG group images. We then generated a weight map (w_i) for every ith IDG group image as:

$$w_i = \frac{\sum_n \frac{1}{2}(B_{xx} + B_{yy})}{n}, \quad (1)$$

which corresponds to the average of the total intensity beam, calculated as the sum of the intensity components along the x-axis B_{xx} and y-axis B_{yy}, across all n observations in each group.

We then used SWARP (Bertin et al. 2002) to co-add the images, creating an extended mosaic for every 20 × 7.68 MHz frequency channel. Furthermore, we also formed a wide-band 60 MHz mosaic over 170–231 MHz for optimal sensitivity and resolution for the source-finding process, as described in Section 4; we created additional 5 × 30.72 MHz mosaic images to enhance the S/N and increase the detectability of fainter sources, thereby enabling more accurate estimates of their spectra. For each of the five bands, we then provide the corresponding four 7.68 MHz sub-band mosaics and one 30.72 MHz mosaic, along with an additional wideband image combining the top two frequency bands (170–231 MHz). To ensure a smooth co-addition, we down-weighted the edges of the weight maps to avoid hard cuts in the mosaics by using a declination-dependent sigmoid function $(1/(1 + \exp^{-(\mathrm{Dec}-\mathrm{Dec_{ref}})}))$.

All mosaics have been corrected for the blurring effect that can arise due to residual ionospheric distortions, following the method of Hurley-Walker et al. (2017). We first selected compact sources from the reference catalogue (introduced in Section 3.3) with $S/N > 10$. We performed an initial source-finding on the mosaics using AEGEAN with a seedclip of 10σ. We then cross-matched the reference sample to the output catalogue form AEGEAN; the size and shape of these sources are then measured from the GP mosaics. We used these sources to determine the PSF map. The process involved interpolating over the sources utilising a Healpix projection (corresponding to pixels roughly 3° across) and averaging each pixel with its neighbours. A smooth map of the major and minor axes, position angle and 'blur' factor is obtained, where the latter corresponds to the ratio between the measured PSF volume and the expected PSF volume from projection effects alone. We multiply the final mosaic by this (position-dependent) factor to normalise the flux density scales so that the peak and integrated flux densities are consistent. Over Galactic latitudes $|b| < 4°$, there

https://doi.org/10.1017/pasa.2025.10094 Published online by Cambridge University Press

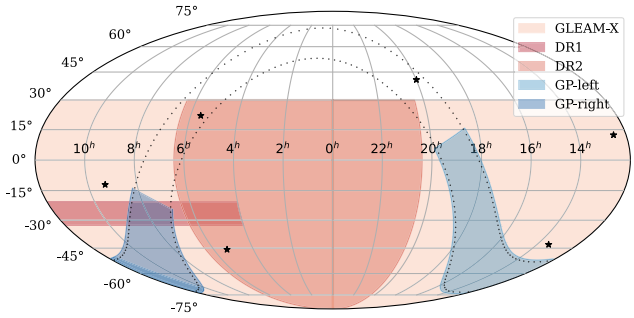


Figure 3. Sky coverage of the GLEAM-X survey, with the light orange region indicating the total area observed. The dark red region represents the area covered in the first data release (DR1; Hurley-Walker et al. 2022), and the light red region highlights the area covered by the second data release (DR2; Ross et al. 2024). In contrast, in light and dark blue are reported the area covering $290° < l < 44°$ and $233° < l < 324°$ respectively, presented in this data release (GP-left, GP-right). The black stars indicate the location of bright radio sources listed from left to right as they appear on the map: Hydra A, Crab, Pic A, Cygnus A, Centaurus A, and Virgo A. The black dotted line shows the GP within $|b| < 10°$.

are insufficient point-like sources, so we perform an interpolation of the PSF components (a_{PSF}, b_{PSF}, PA) and the blur factor.

In order to minimise distortions caused by projection effects, the mosaics have been generated in two sky regions covering $290° < l < 44°$ and $233° < l < 324°$, within latitudes of $|b| < 11°$, using zenithal equal area (ZEA) projection. This maintained a consistent, equatorial-coordinate PSF, which simplifies the formation of a source catalogue (Calabretta & Greisen 2002). The regions of the sky covered in this data release and in the previous two GLEAM-X releases are presented in Figure 3, where the sky coverage of the whole GLEAM-X survey is highlighted in light orange. In addition, the two regions have been mosaicked together using Galactic coordinates for a complete view of the diffuse structures of the GP.

The 26×2 mosaics generated in Section 3.5 comprise a total of 1 898 2-min observations across the two regions. Overall, the sky area covered spans $233° < l < 44°$ and latitudes of $|b| < 11°$, as represented in Figures 4 and 5. We limited the surveyed sky primarily driven by two factors. First, the longitude range accounts for observational constraints, particularly the elevation limits in the northern hemisphere and the presence of Cygnus A, which affects the deconvolution and calibration quality. Sensitivity also decreases at low elevations, making further extensions less effective. We limited the latitude range to $|b| < 11°$ because the joint deconvolution approach is relatively complex, and the extragalactic sky is more easily processed using the basic pipeline (Ross et al. 2024; Ross et al. in preparation). The total area of the data released here is $\approx 3\,800$ deg^2.

3.6 Noise levels

We now analyse the noise properties of the wide-band image to verify that it is Gaussian, a necessary condition for accurate source characterisation. We follow the procedure of Hurley-Walker et al. (2019), Ross et al. (2024), applying it separately to the two regions of the GP: $290° < l < 44°$ and $233° < l < 324°$. For each region, we used a representative 16 deg^2 cutout with a small mean RMS noise of 6 and 3 mJy beam^{-1}, respectively for $290° < l < 44°$ and $233° < l < 324°$, and typical source distribution. The 16 deg^2 cutouts are located outside the plane to avoid contamination from bright diffuse structures and are centred at coordinates of $l, b = (16.4°, -6.6°)$ degrees and $l, b = (301.6°, -7.9°)$ degrees.

We extract the cutout images from the mosaic at 170–231 MHz, generating background and RMS maps using BANE. We subtract the background from the images and perform source extraction with AEGEAN. The source catalogue derived from these images is subsequently subtracted or masked using AERES from the background-subtracted images. In Figure 6, we show the histogram of pixel distribution for the background-subtracted images and the same distribution with faint sources masked and source-subtracted for both the regions of our analyses. The histogram visually assesses the effectiveness of the subtractions applied.

The noise values we obtain at the low latitudes are 5–8 times lower than the GLEAM data published by Hurley-Walker et al. (2019), thanks to the higher resolution of the GLEAM-X survey provided by the longer baselines of the MWA Phase-II extended configuration, and the $\sim 3\times$ longer total integration time processed in this work. This combination ensures that we do not hit the classical confusion limit. RMS noise levels as a function of longitude across the frequency coverage are shown in the Appendix 2 for additional insight into the image quality.

4. Catalogue

We used the same technique described in Hurley-Walker et al. (2019a, 2022) to construct a source catalogue; we briefly summarise the process's main steps. We first measured the background and RMS maps of the wide-band image using BANE. The grid size in the BANE call has been doubled from the default value to account for bright extended structures along the GP, particularly around the Galaxy's centre. A higher grid size value reduces the chances of subtracting the signal from the diffuse structures as background by estimating it over a larger area.

AEGEAN is run with a seedclip of 4σ to find sources in the wide-band image to create a first source list. We applied a global rescaling to match the GLEAM reference catalogue to ensure a consistent flux density scale across the mosaicked images. The source positions from this list are then used to measure sources in the narrow band images (8 MHz wide) using a technique called 'priorised' fitting (see Hancock et al. 2018, for further details on the process), which takes into account the position-dependent PSF for each image. The list is filtered to retain only sources with peak flux densities $\geq 5\times$ the local RMS. These steps were performed in both regions, where we divided the GP, producing two catalogues with a substantial overlap region. We introduced six groups in common across both regions for mosaic generation, ensuring an overlap of $\approx 34°$ in longitude. This approach was chosen to maintain consistent image quality and to establish a clear boundary between the two mosaics, allowing for easy and reliable source selection from the catalogues. To merge the two catalogues, we then selected a hard boundary at a longitude of 309 degrees: if a source is located at a lower longitude, we consider the source from the $290° < l < 44°$ source list; otherwise, if it falls to a higher value, we retain the entry from the $233° < l < 324°$ source list. The final catalogue contains 98 207 radio sources.

Caution needs to be taken when working with sources within $|b| < 1°$, for which BANE does not properly isolate the background levels. Figure 7 illustrates a region of ≈ 16 deg^2 from the 170–231 MHz image, along with its background and RMS maps, and the same sky area as observed by GLEAM (Hurley-Walker et al. 2019a). Although there is an increase in the number of detected

https://doi.org/10.1017/pasa.2025.10094 Published online by Cambridge University Press

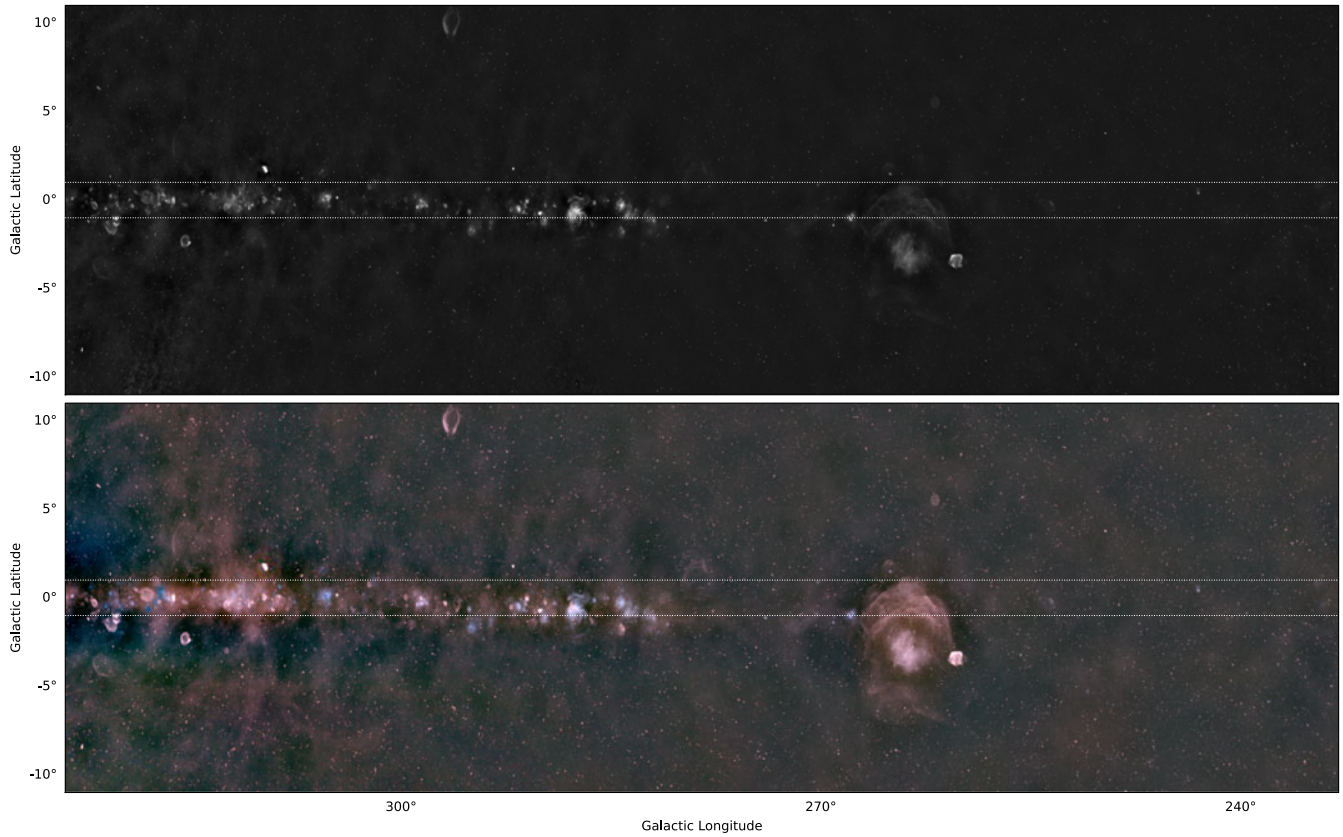


Figure 4. The wide-bandwidth images from the data described in this paper; this illustrative figure shows the $233^\circ < l < 324^\circ$ region. The top panel shows the 170–231 MHz. The bottom panel shows an RGB cube formed of the 72–103 MHz (R), 103–134 MHz (G), and 139–170 MHz (B) data. Dotted white lines indicate $|b| < 1^\circ$. The colour ranges used are -0.025–1.0 Jy beam^{-1} and -0.095–1.25 Jy beam^{-1} with an arcsinh stretch for the two panels, respectively.

sources compared to the previous survey, rising from ≈ 90 to ≈ 300, users are cautioned to carefully examine the flux density values reported in the catalogue and interpret them in context with the images.

4.1 Spectral fitting

We also performed spectral fitting, following the procedure described by Ross et al. (2024), and report the fit spectral energy distributions (SEDs) parameters of sources from the catalogue. Thanks to the 'priorised' fitting approach (Section 4), we were able to extract flux densities across the 20 narrow bands. We applied two spectral models: a simple power law parametrised as $S_\nu = S_{\nu_0}(\nu/\nu_0)^\alpha$, and a curved power law, obtained by multiplying S_ν by $\exp(q\ \ln(\nu/\nu_0)^2)$ where q is related to convex or concave curve respectively for positive or negative values. We used a curved power law to estimate the sample's possible peaked-spectrum sources (PSS). The model selection is based on reduced-χ^2 values; if both models fit well, the one with the lower reduced-χ^2 is chosen. A simple power law successfully fitted 89 655 sources presenting at least 15 integrated flux density measurements with a χ^2 goodness-of-fit above 99% likelihood confidence; the other 3 132 were fitted with a curved spectrum after satisfying the condition of having a reduced-χ^2 lower compared to the reduced-χ^2 for a power law model and having $q\ \Delta q \geq 3$ with $|q| > 0.2$. Figure 8 displays example SEDs for each model. The flux densities used in the SEDs and the spectral indices obtained are consistent with those reported in the GLEAM-GP catalogue, as discussed in Section 4.4, validating the flux scale across the full frequency range.

We estimated the median spectral indices for different flux density ranges and reported the results in Figure 9. Our findings show an excess of steep-spectrum sources along the GP, particularly towards the Galactic centre, with a systematic difference in spectral index between the longitude ranges. By combining data from NVSS at 1 400 MHz and the Tata Institute for Fundamental Research GMRT Sky Survey (TGSS, Intema et al. 2017) at 147 MHz, de Gasperin, Intema, & Frail (2018) analysed this trend in detail, suggesting excess steep-spectrum sources originate from undiscovered radio pulsars, probably missed from past searches due to scattering along the line of sight caused by turbulent ionised gas that broadens the observed pulsation width beyond detectability with traditional time-domain surveys.

4.2 Astrometry

To characterise the precision of the final catalogue, we use the reference list described in Section 3.3 to cross-match with a subset of the GP source catalogue at 200 MHz and determine the offsets in their position. The subset comprehends sources with a high signal-to-noise ratio (≥ 10; hereafter referred to as S/N), isolated (with no internal matches within 10' and unresolved $((a_{src} \times b_{src})/(a_{PSF} \times b_{PSF}) < 1.1)$. The density distribution of the

https://doi.org/10.1017/pasa.2025.10094 Published online by Cambridge University Press

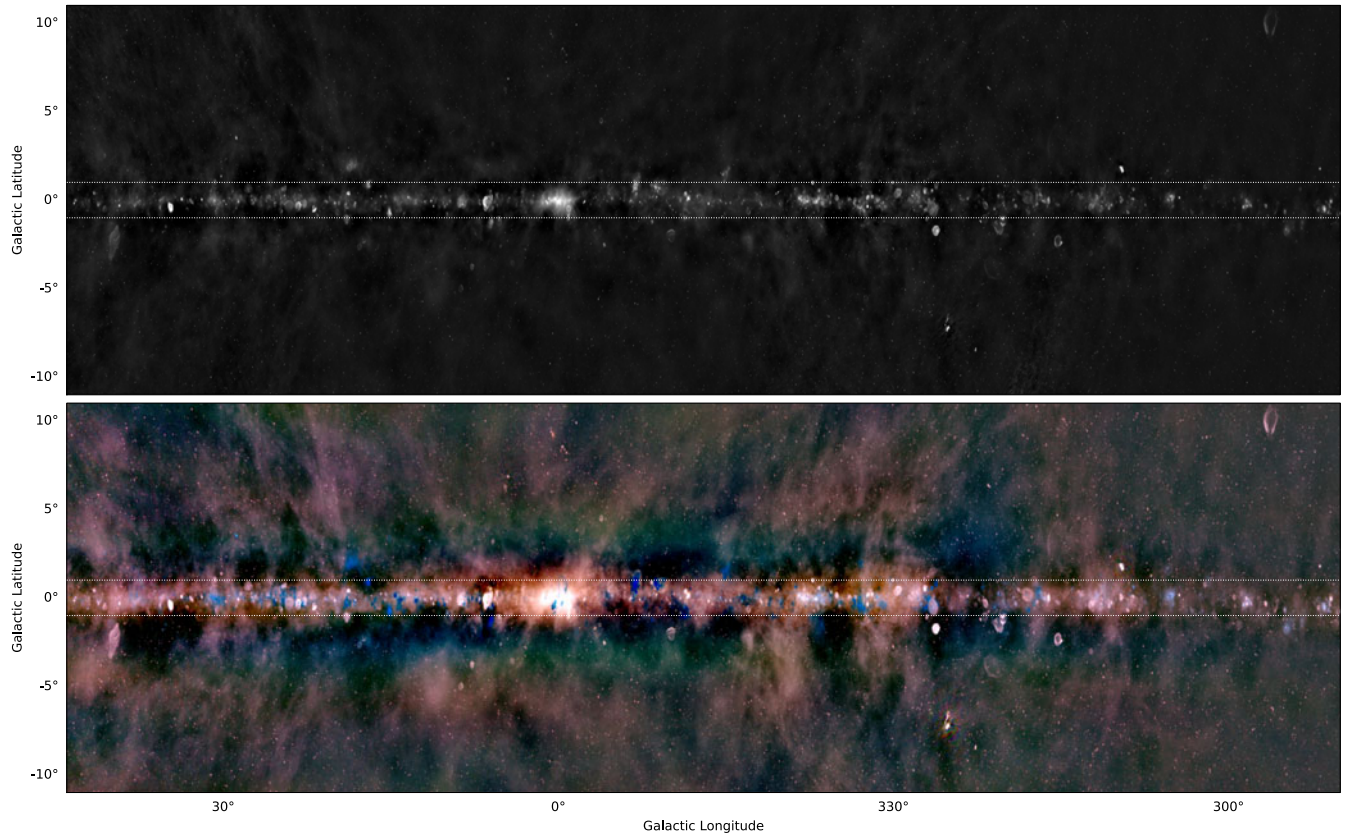


Figure 5. The wide-bandwidth images from the data described in this paper; this illustrative figure shows the $290^\circ < l < 44^\circ$ region. The top panel shows the 170–231 MHz. The bottom panel shows an RGB cube formed of the 72–103 MHz (R), 103–134 MHz (G), and 139–170 MHz (B) data. Dotted white lines indicate $|b| < 1^\circ$. The colour ranges used are -0.025–1.0 Jy beam^{-1} and -0.095–1.25 Jy beam^{-1} with an arcsinh stretch for the two panels, respectively.

astrometric offsets is shown in Figure 10. The average RA and Dec astrometric offsets, with respect to the reference list, are -148 ± 980 mas and $+7 \pm 980$ mas, respectively.

4.3 Reliability and completeness

To assess the reliability of our catalogue, we performed the same analysis as Hurley-Walker et al. (2022) and Ross et al. (2024). The procedure checks for false detections and was conducted separately for the $290^\circ < l < 44^\circ$ and $233^\circ < l < 324^\circ$ regions. We limit the reliability and the following completeness simulations to $4^\circ < |b| < 11^\circ$ as we do not expect them to be accurate in the presence of the bright diffuse structures of the GP.

To estimate the reliability of our source catalogue, we run AEGEAN to detect negative sources in the mosaics using the same setting described in Section 4. Since real sources cannot have negative flux, these detections reflect noise and artefacts, allowing us to estimate the false detection rate. We then applied two filtering criteria. The first accounts for artefacts generated by very bright sources, which produce positive and negative features around themselves. These detections have been filtered out (positive and negative), accounting for the decreasing brightness of the artefacts as the distance from the source increases. This single-filter curve serves as a lower limit for the reliability of the catalogue. We then applied a second filter to the negative detections to discard all the elements within 2′ of positive sources, likely generated by residual calibration errors. In total, we identified 156 negative sources within $290^\circ < l < 44^\circ$ and 250 in $233^\circ < l < 324^\circ$, resulting in an estimated catalogue reliabilities of 99.3% and 99.4%, respectively. The reliability for each significant bin is illustrated in Figure 11.

We then applied the same approach implemented in the previous GLEAM (Hurley-Walker et al. 2017) and GLEAM-X (Hurley-Walker et al. 2022; Ross et al. 2024) surveys to quantify the completeness of the catalogue at 200 MHz, which is the band used for source-finding, for the $290^\circ < l < 44^\circ$ and $233^\circ < l < 324^\circ$ regions. For each region, 15 000 point sources are simulated within the longitude range of the area covered using 21 realisations, each of which had a different flux density varying from 10^{-2} to 10^0Jy with an increment in the index of 0.1. The simulated sources are chosen in a random position within $4^\circ < |b| < 11^\circ$ and with a minimum separation of 5 arcmin. Their major and minor axes are set to a_{PSF} and b_{PSF}. AERES is then used to inject these sources into the wide-band image.

The same AEGEAN call used to detect sources in the 60 MHz image for the source-finding procedure is applied here. The list of simulated sources recovered by the software is compared to their original sample, and their fraction is calculated to estimate the completeness. Simulated sources that lie close to a real source are considered successful only when the recovered position falls closer to the simulated source rather than the nearby real source.

The completeness is estimated to be 50% at ≈ 25 mJy and increases to 90% at 50 mJy in the $233^\circ < l < 324^\circ$, while for the $290^\circ < l < 44^\circ$ region it corresponds to 50% at ≈ 15 mJy and rising to 90% at 125 mJy. The fraction of the simulated sources as a

https://doi.org/10.1017/pasa.2025.10094 Published online by Cambridge University Press

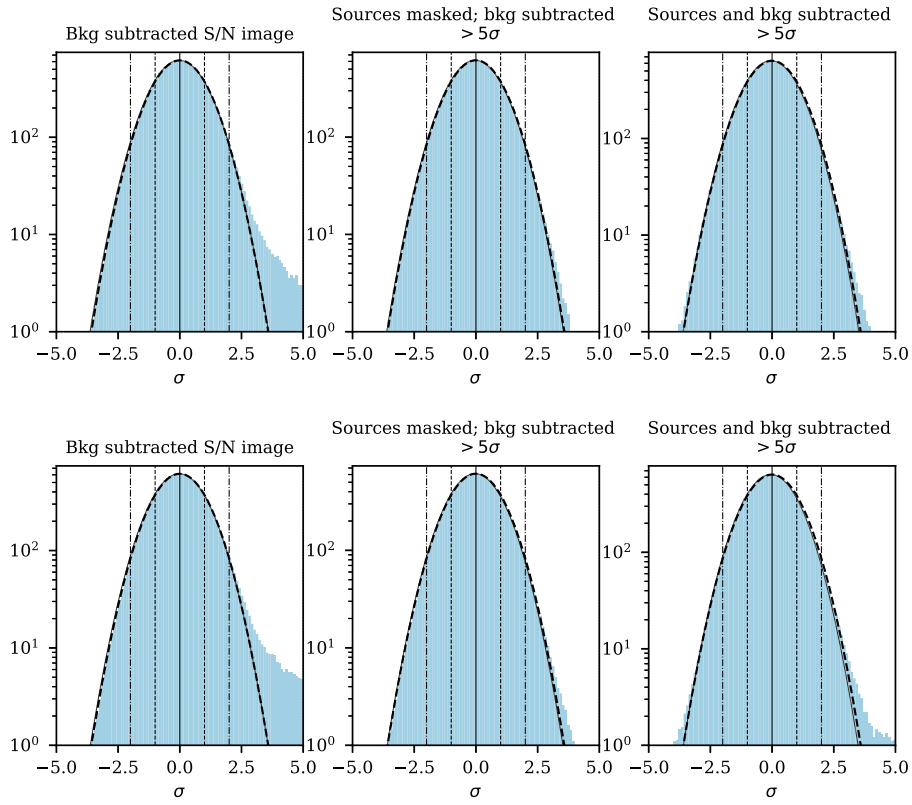


Figure 6. Pixel distribution for a 16 deg^2 region of the wide-band source finding image covering 170–231 MHz. The top row correspond to the region centred in $l, b = (16.4^\circ, -6.6^\circ)$ for $290^\circ < l < 44^\circ$, while the bottom row corresponds to the region centred in $l, b = (301.6^\circ, -7.9^\circ)$ for $233^\circ < l < 324^\circ$. The RMS noise levels, determined using BANE, are 6 and 3 mJy beam^{-1}, respectively. Each figure consists of three panels: the leftmost panel shows the distribution of pixel S/N values after subtracting the background and dividing by the RMS noise map. The central and right panels show the same distribution but are limited to sources $> 5\sigma$ with faint sources masked using AERES (central panel) or subtracted (right panel). The black solid line represents a Gaussian distribution with $\sigma = 1$ (as measured by BANE, while the black dashed line is a fitted Gaussian to the pixel distribution. Vertical solid lines indicate the mean values; dashed lines correspond to $|S/N| = 1\sigma$; and dash-dotted lines correspond to $|S/N| = 2\sigma$.

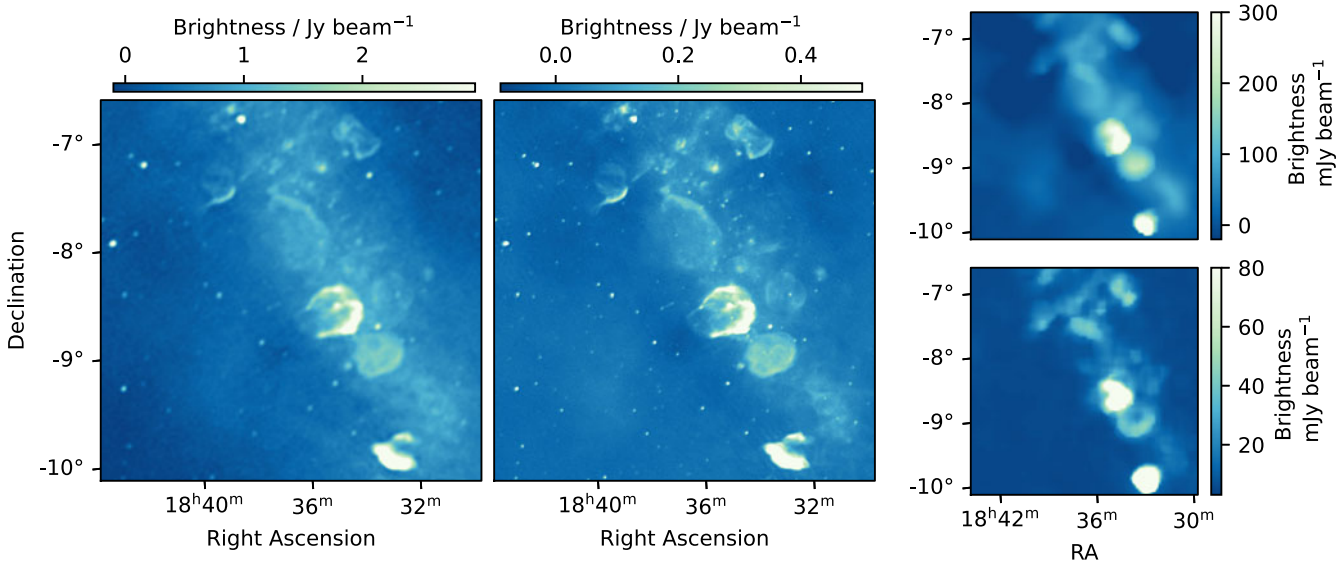


Figure 7. ≈ 16 deg^2 from the 170–231 MHz mosaic of GLEAM and this work centred on RA 18h36m and Dec −8°. The region, as seen by GLEAM, is reported in the left panel; the middle shows the wide-band image of this work; and the small panels on the right represent the background (top) and RMS (bottom) maps of the wide-band image. The median RMS is 657 and 103 mJy beam^{-1} in GLEAM and this work, respectively. AEGEAN detected ≈ 90 and ≈ 300 sources in GLEAM and in this work.

https://doi.org/10.1017/pasa.2025.10094 Published online by Cambridge University Press

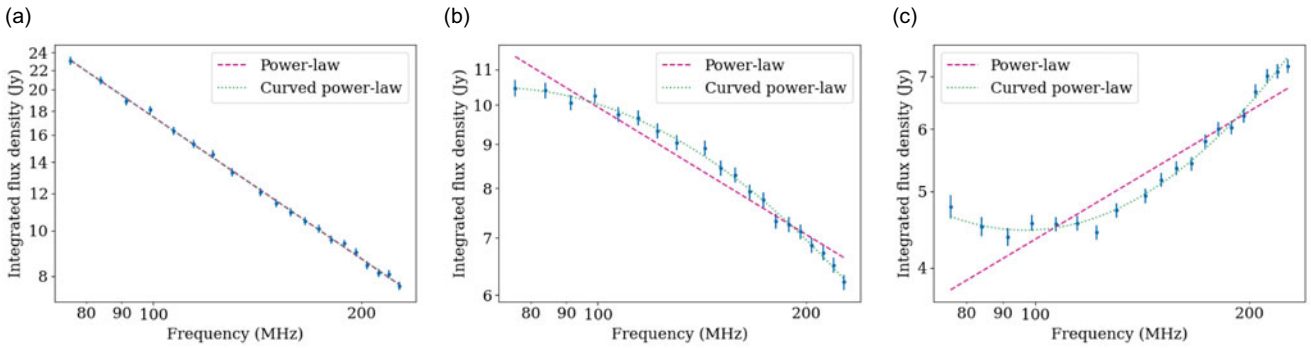


Figure 8. Example SEDs for the narrow band measurements of three unresolved point sources. (a) shows a standard power law spectrum, (b)–(c) show convex and concave curved power-law spectra, respectively. The spectral model has been selected by the criteria listed in Section 4.1.

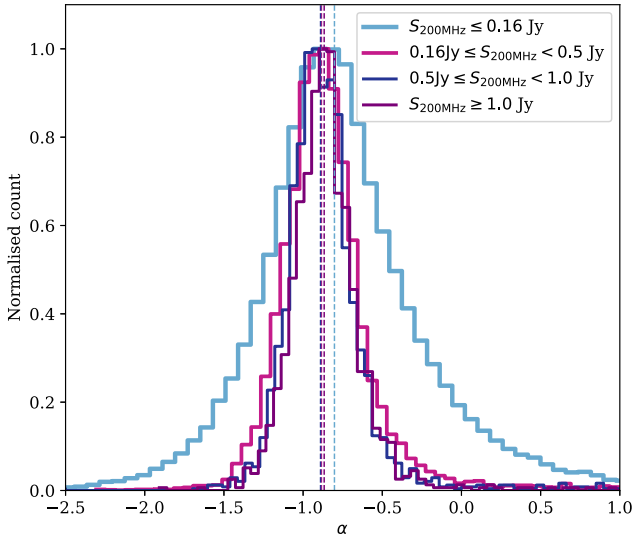


Figure 9. Distribution of the spectral index α as a function of the flux density. The cyan line shows sources with $S_{200\,\mathrm{MHz}} < 0.16$ Jy, the magenta line shows sources with $0.16\ \mathrm{Jy} \leq S_{200\,\mathrm{MHz}} < 0.5$ Jy, the blue line shows sources with $0.5\ \mathrm{Jy} \leq S_{200\,\mathrm{MHz}} < 1.0$ Jy, and the purple line shows sources with $S_{200\,\mathrm{MHz}} \geq 1.0$ Jy. The dashed lines of the same colour highlight the median value for every flux density bin, and they respectively correspond to −0.80, −0.87, −0.88, and −0.86.

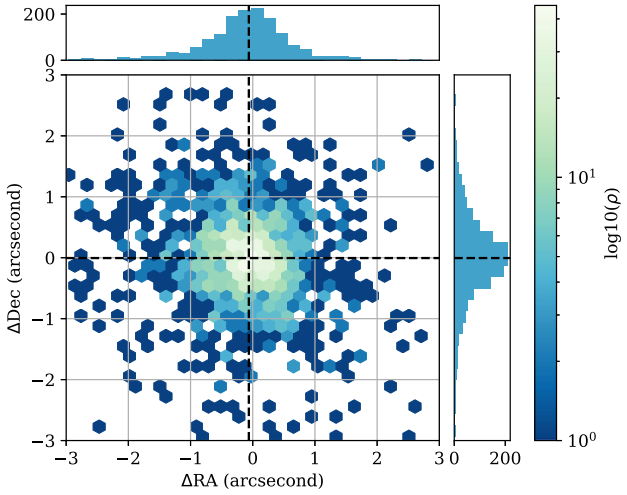


Figure 10. The astrometric offsets of 8 421 sources which are isolated, compact, and > 10 σ after they have been cross-matched against the reference catalogue described in Section 3.3. Black vertical and horizontal lines correspond to the mean offset in the RA and Dec directions and have a value of -148 ± 980 mas and $+7 \pm 980$ mas, respectively. Histograms show the counts for the astrometry offset measures in each direction. The colour bar represents the density of points (ρ) on a logarithmic scale.

function of the S_{200MHz} is reported in Figure 12 for both regions. The error bars reflect variations in completeness across the GP. In the longitude range $233° < l < 324°$, the error bars are relatively small, indicating uniform completeness throughout the region. In contrast, the region $290° < l < 44°$ shows larger error bars due to significant variations in completeness, ranging from a relatively quiet area near the Vela SNR and beyond to a much noisier region influenced by the presence of Centaurus A.

4.4 Comparison with GLEAM-GP

We use the GLEAM-GP data to calibrate flux density during data reduction (Section 4). We now compare the GLEAM-GP dataset to the GP catalogue presented here to examine any differences that might be in place between these two surveys. For this purpose, we considered only the available GLEAM-GP catalogue (Hurley-Walker et al. 2017) covering $345° < l < 67°$, $180° < l < 240°$ and galactic latitudes $1° < |b| < 10°$. For the comparison, we select a compact subset of sources ($S_{\mathrm{int}}/S_{\mathrm{peak}} < 2$), that are well described by a power law (reduced-$\chi^2 < 1.93$, equivalent to a 99% confidence level) and cross-matched within a radius of 15″. We additionally correct the GLEAM-GP data for the Eddington bias, which involves the flux density of faint sources being systematically biased high due to the noise (Eddington 1913). Following the approach of Hurley-Walker et al. (2022), we apply the correction from equation 4 of Hogg & Turner (1998) to estimate the true flux density of GLEAM-GP sources at 200 MHz to ultimately verify the GP flux density scale:

$$S_{corr} = \frac{S_0}{2}\left(1 + \sqrt{1 - \frac{4q+4}{S/N^2}}\right) \tag{2}$$

https://doi.org/10.1017/pasa.2025.10094 Published online by Cambridge University Press

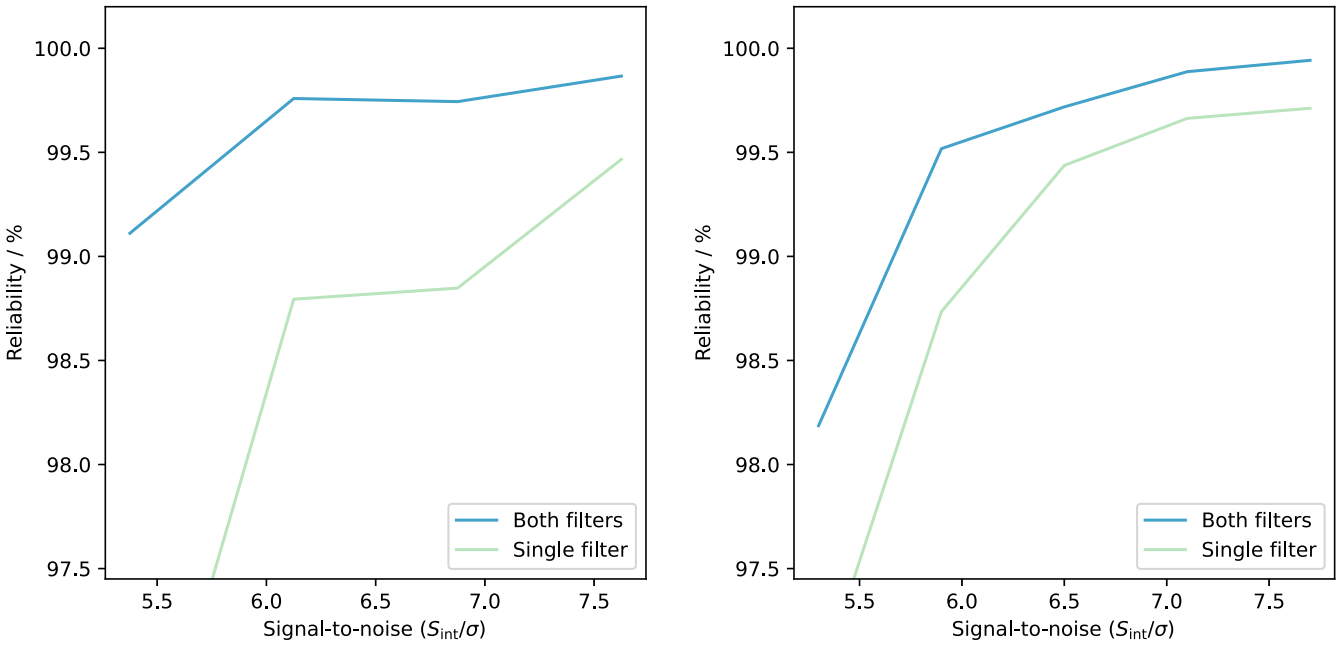


Figure 11. Estimates of the reliability of the catalogue as a function of the S/N. The left panel corresponds to $290^\circ < l < 44^\circ$, while the right panel corresponds to $233^\circ < l < 324^\circ$. In both panels, the lower green line is a conservative estimate before filtering out the sample near bright, positive sources. The upper blue curve is derived after these sources have been filtered out.

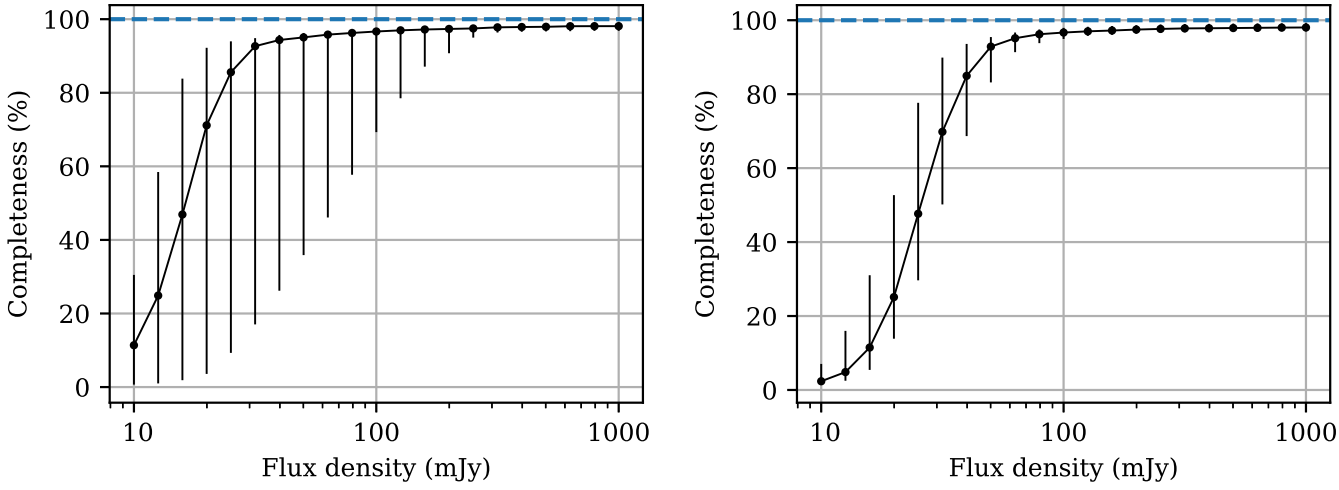


Figure 12. Estimates of the catalogue's completeness as a function of $S_{200\,\mathrm{MHz}}$. The left panel corresponds to $290^\circ < l < 44^\circ$, while the right panel corresponds to $233^\circ < l < 324^\circ$. The error bars are due to variations in completeness with dependence on l because of the presence of bright sources.

where q represents the number of sources to flux ratio in logarithmic scale and assumes a value of 1.54. The integrated flux density ratio is then calculated and shown in Figure 13 with the correction applied to the GLEAM flux densities. The line in black indicates the best trend for the fluxes, as expected around 1.

We also compare spectral indices derived from a power law model between our GP catalogue and the published GLEAM-GP (after excluding all the sources with α set to 0 because we cannot find an optimal fit). The trend is shown in Figure 14 and has the expected behaviour. In the bottom right corner of the illustration, we include the errors for both datasets: our GP catalogue shows significantly smaller errors due to the increased S/N in this sky area, thanks to the introduction of GLEAM-X observations. We are then confident in the spectral fitting for the given sources.

A detailed comparison of the Galactic centre is presented in Figure 15, highlighting the improved image quality relative to the GLEAM survey (Hurley-Walker et al. 2019). Thanks to the inclusion of GLEAM-X observations, the new image shows a significant noise reduction, resulting in a cleaner background and a more distinct representation of structural features, offering a more precise view of its intricate components.

https://doi.org/10.1017/pasa.2025.10094 Published online by Cambridge University Press

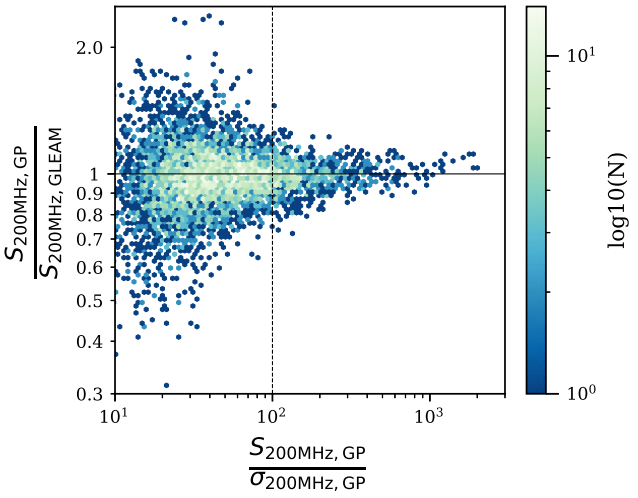


Figure 13. Ratio of the 200 MHz integrated flux density for compact sources matched in the GP catalogue presented here and GLEAM-GP as a function of the S/N in our sample. The vertical dashed line marks a S/N of 100, corresponding to approximately 90% completeness in GLEAM. The horizontal solid line represents a ratio of 1, aligning with the overall trend. Colour indicates point density. Error bars are omitted for clarity but are calculated as the quadrature sum of measurement errors from both surveys.

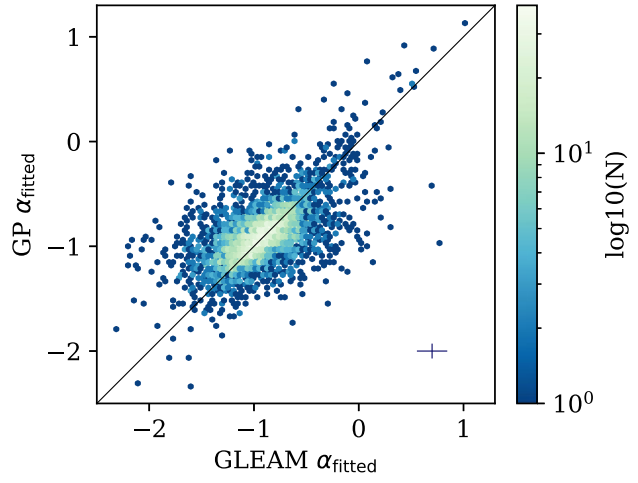


Figure 14. Spectral indices derived from a power law spectral model across the 20 × 7.68 MHz narrow bands for compact sources matched in the GP catalogue presented here and GLEAM. The colour scale represents the density of points, and the average fitting error is shown as an error bar in the bottom right. The diagonal line indicates a 1:1 correspondence of α.

5. Science applications

5.1 Supernova remnants

The frequency coverage within 72–231 MHz combined with the sky area covered by this data release will likely be productive for studies of SNRs (see Dubner & Giacani 2015, for a review) in our Galaxy. SNRs go through four stages during their lifetime, where they exhibit different spectral behaviours according to the particle acceleration mechanisms that are taking place, how they interact with the surrounding medium, and finally, the amount of energy they are losing. Along the GP, we expect to observe ≈ two thousand SNRs (Frail, Goss, & Whiteoak 1994). However, the actual number of objects we have been able to classify is around 300 (Green 2024), less than half compared to the theoretical estimate. The lack of detections is likely caused by the limitations of previous radio surveys in terms of sky coverage and sensitivity to large scales. MWA has proven to be highly effective in detecting SNRs (Hurley-Walker et al. 2019b; Mantovanini, Hurley-Walker, & Anderson 2025a) due to its sensitivity to low-frequency radio emission, and thanks to the broad range of angular scales that we could recover ($45'' - 15°$), we are confident this data release will help find more faint and old elements of the SNR population, helping to fill the current gap.

Furthermore, the sensitivity of our GP image will allow us to confidently measure the flux density of sources with an angular size up to a few degrees over a wide frequency band. It will enable detailed spectral fitting, essential in confirming the nature of the sources. We provide an example of the well-known G18.8 + 0.3 (also known as Kes67) spectra in Figure 16. In addition, as highlighted by Castelletti et al. (2021), these lower frequencies can provide insights into the physical properties of the observed regions, particularly for possible free-free absorption occurring inside or outside the remnant shell, which can be respectively caused by the presence of unshocked ejecta (see Arias et al. 2018, for a similar investigation) or interaction with the surrounding environment (such as molecular clouds). In this regime, SNRs are better described by a power law with a turnover at frequencies < 100 MHz (as first stated by Dulk & Slee 1975).

On the other hand, the spectra of SNRs at radio frequencies are connected to gamma-ray emissions, particularly in the context of SNRs as potential sources of Galactic cosmic rays (CR) at very high energies (up to PeV; further details in Cristofari, Blasi, & Amato 2020). Therefore, the radio spectrum can constrain the efficiency and nature of electron acceleration within SNR shocks. Since the processes driving proton acceleration are expected to be similar, radio studies are also relevant to investigations into the origin of CRs (as outlined in Dubner & Giacani 2015, and references therein). It is then worth looking for possible associations between gamma rays and SNRs (Maxted et al. 2019). The GP image could be crucial in identifying faint radio structures previously gone unnoticed, with which a gamma-ray source may be associated.

5.2 HII regions

HII regions are mostly formed by the ionisation of the medium due to the ultraviolet radiation emitted by a newly born star (Condon & Ransom 2016); as such, they represent good tracers for star formation regions in the galaxy. These sources have been mostly identified at infrared (IR) wavelength; the Widefield Infrared Survey Explorer (AllWISE; Wright et al. 2010; Mainzer et al. 2011) have been extensively used, where all sources show essentially the same morphology: at $\simeq 22\,\mu m$, the main contribution to the emission is caused by the radiation of hot dust, and it is surrounded by a ring at $\simeq 12\,\mu m$ caused by Polycyclic Aromatic Hydrocarbon molecules excited by UV radiation from the nearby stars (Watson et al. 2008). The ionised gas is visible at radio frequencies, which are then used to confirm the identification of a HII region.

HII regions are typically dominated by thermal free-free emission with a spectral index between $-0.2 < \alpha < +2$. They become optically thick at low radio frequencies (below 100 MHz), which means that the diffuse non-thermal emission of the background

https://doi.org/10.1017/pasa.2025.10094 Published online by Cambridge University Press

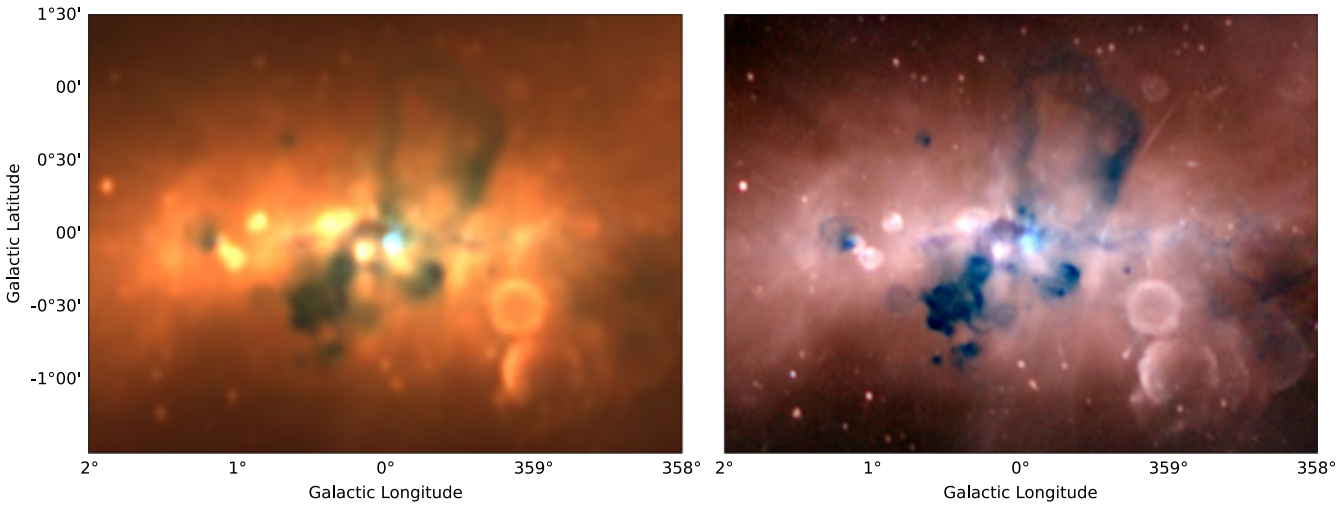


Figure 15. RGB cubes of the Galactic Centre as seen by GLEAM (left panel; see Hurley-Walker et al. 2017; Hurley-Walker et al. 2024, for a detailed analysis) and by this data release (right panel). The cubes have been formed of the 72–103 MHz (R), 103–134 MHz (G), and 139–170 MHz (B) data. The colour ranges used are −0.5–20 and −0.12–5 Jy beam^{-1} for the two panels, respectively.

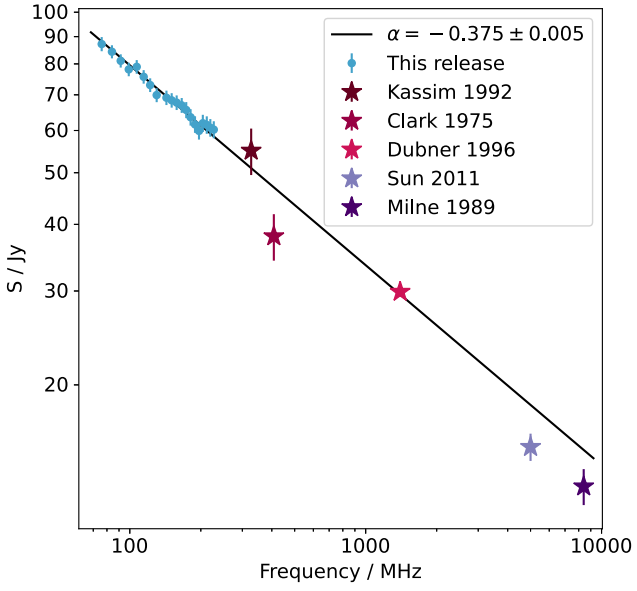


Figure 16. Radio continuum spectrum for G18.8 + 0.3 (Kes67) in logarithmic scale. The blue circles indicate the narrow band's flux density measurements presented in this work between 72–231 MHz, while in other colours, the published measurements reported by Green (2024) in the SNR catalogue from work by: Kassim (1992) at 327 MHz, Clark et al. (1975) at 408 MHz, Dubner et al. (1996) at 1 400 MHz, Sun et al. (2011) at 5 000 MHz, and Milne et al. (1989) at 8 400 MHz. Where errors were not specified in the original papers, we assumed them to be 10% of the flux density. The solid line represents the best-fitting curve.

is absorbed. This effect is visible in our observations. We constructed an RGB cube composed of the 72–103 MHz (R), 103–134 MHz (G), and 139–170 MHz (B) images, as shown in the top panel of Figure 17. HII regions are immediately recognised by a distinctive blue colour in opposition to the non-thermal emission, which appears red due to its negative spectral index. The boxes represent three known objects, and their appearance at IR wavelengths is shown in the smaller panels of the second row. The different colours will be crucial in disentangling the emission's origin, particularly in SNR identification, for which these thermal sources are often a source of confusion (Helfand et al. 2006; Hurley-Walker et al. 2019a).

Hindson et al. (2016) leveraged their distinctive blue colour to compile a comprehensive catalogue using GLEAM data over the longitude range $340° < l < 260°$. The final result has been implemented (see Polderman et al. 2019; Polderman et al. 2020) to measure the synchrotron radiation emitted along the line of sight (the so-called synchrotron emissivity ϵ) in front and behind absorbed HII regions. A broader study by Su et al. (2018) mapped the synchrotron emissivity throughout the Galaxy using 152 HII regions. By deriving optical depths, the authors achieved more precise estimates of how much radiation each object absorbs, enabling more reliable measurements of ϵ. The synchrotron emissivity is directly related to the density of CR electrons and the strength of the GMF component perpendicular to the line of sight. The approach then manages to constrain the CR population and the structure of the GMF across the plane. However, it is challenging to disentangle the contribution of each component, and precise models are necessary to address this degeneracy and understand their role in our galaxy's constitution. The increased resolution and sensitivity of the GP survey presented here may be essential in detecting more absorption features and enabling emissivity calculation over a wider range of lines of sight.

5.3 Planetary nebulae

Planetary nebulae (PNe) mark the final evolutionary stages of low to intermediate mass (∼1–8 $M_\odot$) stars. The large stellar winds from these stars, while in the asymptotic giant branch (AGB) phase, result in significant mass loss. Radio continuum observations of PNe reveal the thermal free-free emission from ionised outflows, and are not limited by the dust extinction in the Milky Way like optical observations (Pazderska et al. 2009; Chhetri et al. 2015). PNe typically become optically thin with a spectral peak at frequencies dependent on the age and angular size of the PNe.

https://doi.org/10.1017/pasa.2025.10094 Published online by Cambridge University Press

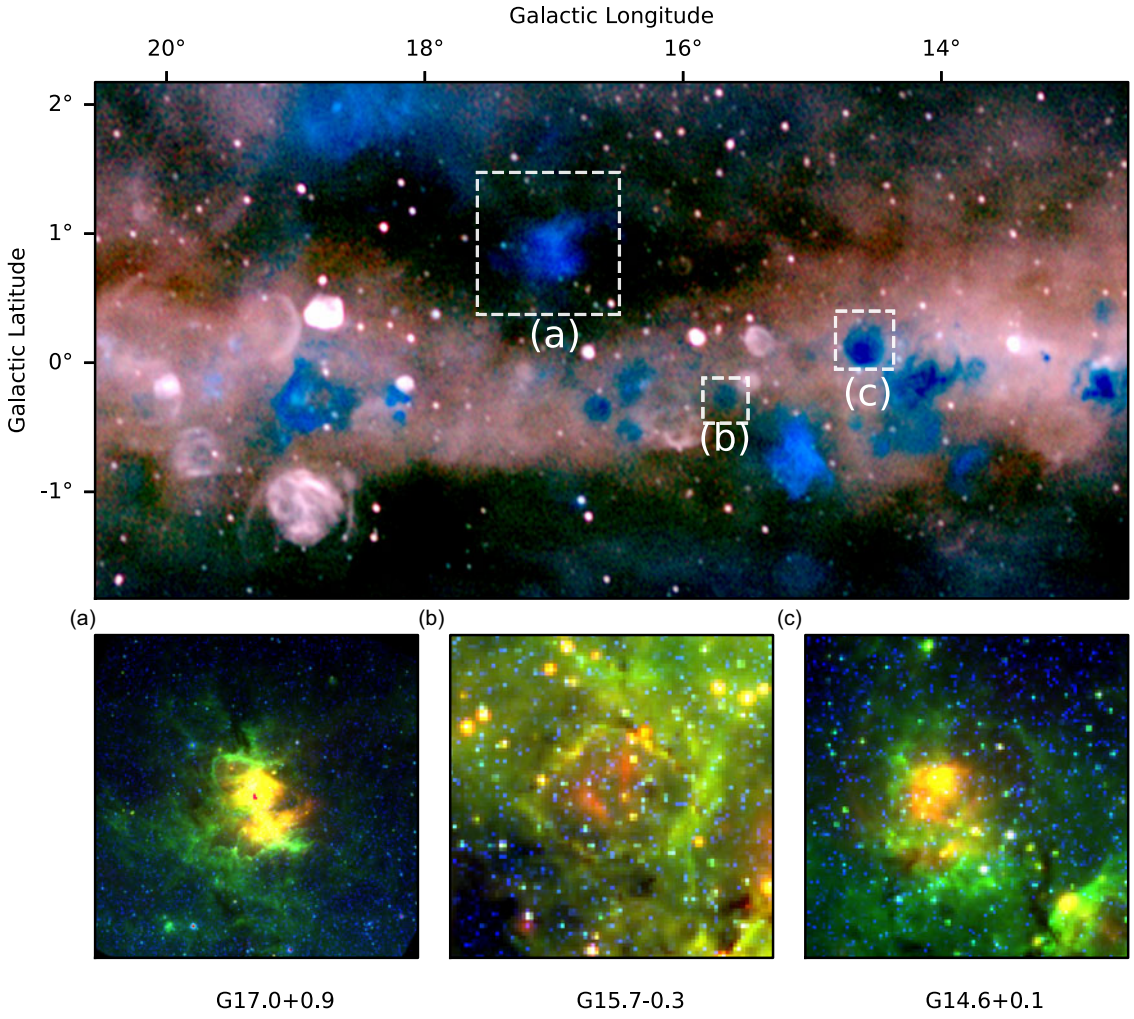


Figure 17. Section of 8° in longitude of the southern GP. The top panel shows an RGB cube formed of processed data from this release: 72–103 MHz (R), 103–134 MHz (G), and 139–170 MHz (B). White squares indicate three examples of known HII regions in the area: G17.0+0.9 (a), G15.7−0.3 (b), and G14.6+0.1 (c). The bottom row shows corresponding objects in AllWISE bands, with the RGB channels assigned to 22 μm (R), 12 μm (G), and 3.4 μm (B).

Characterising radio continuum SEDs, particularly over the spectral peak and optically thick region, can help to characterise the properties of PNe, resolving long-standing tensions between different geometries, density and temperature profiles and velocities. The region included in this data release provides crucial insights into the optically thick frequencies for several known or candidate PNe. For example, NGC 3918 (PN G294.6+04.7), a well known and studied bright PN, is modelled with a power-law spectral model with a spectral index of $\alpha = 1.2$, consistent with previous radio observations (Chhetri et al. 2015).

5.4 Pulsars

Continuum radio images, while less traditional, are a novel way of detecting low-frequency pulsars that may be undetectable in high time resolution searches due to scattering and dispersion, and can provide additional information on the sources, such as accurate flux density measurements. Sett et al. (2024) provide an example of this approach at ≤ 300 MHz, detecting 83 known pulsars, 14 of which were the first reported low-frequency detections, previously missed by periodic searches because located at high Dispersion Measure or highly scattered. A simple power law with a very steep index (on average −1.6 as illustrated by Bates, Lorimer, & Verbiest 2013) is often used to describe pulsars; in 10% of the known pulsars though, it is observed a turnover at low frequencies (below 400 MHz) that may be caused by synchrotron self-absorption or thermal absorption by gas present along the same line of sight of the source (as described in Swainston et al. 2021, 2022, and references therein). Thanks to the frequency range covered in this work, the survey of the GP we are presenting here can be crucial in bringing out the presence of a turnover in the spectra of known pulsars. Murphy et al. (2017) performed similar work on a limited sample of pulsars visible by GLEAM at 200 MHz. (Mantovanini et al. 2025b) show that the reduced confusion noise enabled by introducing GLEAM-X observations increases the percentage of the population visible at these frequencies to examine the overall population better, and provides new pulsar candidates ideal for follow-up pulsation searches at higher frequencies. Furthermore, cross-matching steep-spectrum sources in our catalogue with unassociated gamma-ray sources may reveal

https://doi.org/10.1017/pasa.2025.10094 Published online by Cambridge University Press

additional pulsar candidates (Frail et al. 2018) worth following up in future studies, and an analysis of their eclipsing variability could help identify them as eclipsing binary millisecond pulsars (MSPs; Petrou et al. in preparation).

6. Final remarks

This work provides $\approx 3\,800$ deg^2 of the southern GP as part of the GLEAM-X survey. The 26×2 mosaics cover an area of $233^\circ < l < 44^\circ$ within latitudes of $|b| < 11^\circ$ generated by a combination of 1 898 2-min observations corresponding to the 57% of the total number of processed data. 53% of the successful observations are from GLEAM-X, and 47% from GLEAM. Along with the mosaics, we also provide a source catalogue composed of 98 207 elements, for which 92 787 were successfully fitted either by a simple or curved power law.

Acknowledgement. N.H.-W. is the recipient of an Australian Research Council Future Fellowship (project number FT190100231).

This scientific work uses data obtained from Inyarrimanha Ilgari Bundara, the CSIRO Murchison Radio-astronomy Observatory. Support for the operation of the MWA is provided by the Australian Government (NCRIS), under a contract to Curtin University administered by Astronomy Australia Limited. We acknowledge the Pawsey Supercomputing Centre which is supported by the Western Australian and Australian Governments.

Data availability. All the images and the catalogue are available on Vizier (https://vizier.cds.unistra.fr/viz-bin/VizieR) and on AAO Data Central (https://datacentral.org.au) for download.

References

Anderson, L. D., et al. 2017, A&A, 605, A58
Anderson, L. D., et al. 2025, A&A, 693, A247
Arias, M., et al. 2018, A&A, 612, A110
Bates, S. D., Lorimer, D. R., & Verbiest, J. P. W. 2013, MNRAS, 431, 1352
Bertin, E., et al. 2002, in Astronomical Society of the Pacific Conference Series, Vol. 281, Astronomical Data Analysis Software and Systems XI, ed. D. A. Bohlender, D. Durand, & T. H. Handley, 228
Briggs, D. S. 1995, in American Astronomical Society Meeting Abstracts, Vol. 187, American Astronomical Society Meeting Abstracts, 112.02
Brunthaler, A., et al. 2021, A&A, 651, A85
Calabretta, M. R., & Greisen, E. W. 2002, A&A, 395, 1077
CASA Team, et al. 2022, PASP, 134, 114501
Castelletti, G., Dubner, G., Brogan, C., & Kassim, N. E. 2007, A&A, 471, 537
Castelletti, G., Supan, L., Peters, W. M., & Kassim, N. E. 2021, A&A, 653, A62
Cavallaro, F., et al. 2017, MNRAS, 473, 1685
Chhetri, R., et al. 2015, MNRAS, 451, 3228
Clark, D. H., Green, A. J., & Caswell, J. L. 1975, AuJPS, 37, 75
Condon, J. J., et al. 1998, AJ, 115, 1693
Condon, J. J., & Ransom, S. M. 2016, Essential Radio Astronomy
Cotton, W. D. 2017, PASP, 129, 094501
Cristofari, P., Blasi, P., & Amato, E. 2020, APh, 123, 102492
de Gasperin, F., Intema, H. T., & Frail, D. A. 2018, MNRAS, 474, 5008
Dubner, G., & Giacani, E. 2015, A&A Rev., 23, 3
Dubner, G. M., Giacani, E. B., Goss, W. M., Moffett, D. A., & Holdaway, M. 1996, AJ, 111, 1304
Dulk, G. A., & Slee, O. B. 1975, ApJ, 199, 61
Eddington, A. S. 1913, MNRAS, 73, 359
Frail, D. A., Goss, W. M., & Whiteoak, J. B. Z. 1994, ApJ, 437, 781
Frail, D. A., et al. 2018, MNRAS, 475, 942
Goedhart, S., et al. 2024, MNRAS, 531, 649
Green, D. A. 2024, An updated catalogue of 310 Galactic supernova remnants and their statistical properties, arXiv:2411.03367
Hale, C. L., et al. 2021, PASA, 38, e058
Hancock, P. J., Murphy, T., Gaensler, B. M., Hopkins, A., & Curran, J. R. 2012, MNRAS, 422, 1812
Hancock, P. J., Trott, C. M., & Hurley-Walker, N. 2018, PASA, 35, e011
Helfand, D. J., Becker, R. H., White, R. L., Fallon, A., & Tuttle, S. 2006, AJ, 131, 2525
Hindson, L., et al. 2016, PASA, 33, e020
Hogg, D. W., & Turner, E. L. 1998, PASP, 110, 727
Hotan, A. W., et al. 2021, PASA, 38, e009
Hurley-Walker, N., & Hancock, P. J. 2018, A&C, 25, 94
Hurley-Walker, N., et al. 2017, MNRAS, 464, 1146
Hurley-Walker, N., et al. 2019, PASA, 36, e047
Hurley-Walker, N., et al. 2019a, PASA, 36, e048
Hurley-Walker, N., et al. 2019b, PASA, 36, e045
Hurley-Walker, N., et al. 2022, PASA, 39, e035
Hurley-Walker, N., et al. 2024, ApJ, 969, 42
Ingallinera, A., et al. 2014, MNRAS, 437, 3626
Intema, H. T., Jagannathan, P., Mooley, K. P., & Frail, D. A. 2017, A&A, 598, A78
Intema, H. T., et al. 2009, A&A, 501, 1185
Kassim, N. E. 1992, AJ, 103, 943
Mainzer, A., et al. 2011, ApJ, 731, 53
Mantovanini, S., Hurley-Walker, N., & Anderson, G. 2025a, PASA, 42, e021
Mantovanini, S., et al. 2025b, arXiv e-prints, arXiv:2509.02919
Mauch, T., et al. 2003, MNRAS, 342, 1117
Maxted, N. I., et al. 2019, ApJ, 885, 129
McConnell, D., et al. 2020, PASA, 37, e048
Medina, S.-N. X., et al. 2024, A&A, 689, A196
Milne, D. K., Caswell, J. L., Kesteven, M. J., Haynes, R. F., & Roger, R. S. 1989, PASA, 8, 187
Morgan, J., & Galvin, T. 2021, johnsmorgan/mwa_pb_lookup: Version 1.0, doi: 10.5281/zenodo.5083990
Murphy, T., et al. 2017, PASA, 34, e020
Nord, M. E., Henning, P. A., Rand, R. J., Lazio, T. J. W., & Kassim, N. E. 2006, AJ, 132, 242
Norris, R. P., et al. 2021, PASA, 38, e046
Offringa, A. R., & Smirnov, O. 2017, MNRAS, 471, 301–316
Offringa, A. R., et al. 2014, MNRAS, 444, 606
Pazderska, B. M., et al. 2009, A&A, 498, 463
Polderman, I. M., Haverkorn, M., & Jaffe, T. R. 2020, A&A, 636, A2
Polderman, I. M., Haverkorn, M., Jaffe, T. R., & Alves, M. I. R. 2019, A&A, 621, A127
Ross, K., et al. 2024, arXiv e-prints, arXiv:2406.06921
Sett, S., Sokolowski, M., Lenc, E., & Bhat, N. D. R. 2024, PASA, 41, e045
Sokolowski, M., et al. 2017, PASA, 34, e062
Stil, J. M., et al. 2006, AJ, 132, 1158
Su, H., et al. 2018, MNRAS, 479, 4041
Sun, X. H., et al. 2011, A&A, 536, A83
Swainston, N. A., Lee, C. P., McSweeney, S. J., & Bhat, N. D. R. 2022, PASA, 39, e056
Swainston, N. A., et al. 2021, ApJ, 911, L26
Swarup, G., et al. 1991, CSci, 60, 95
Tingay, S. J., et al. 2013, PASA, 30, e007
van der Tol, S., Veenboer, B., & Offringa, A. R. 2018, A&A, 616, A27
van Weeren, R. J., et al. 2016, ApJS, 223, 2
Watson, C., et al. 2008, ApJ, 681, 1341
Wayth, R. B., et al. 2015, PASA, 32, e025
Wayth, R. B., et al. 2018, PASA, 35, e033
Wright, E. L., et al. 2010, AJ, 140, 1868

Appendix A. Ionospheric activity

As mentioned in Section 3.3, to assess the impact of ionospheric conditions on data quality, we analysed the distribution of pipeline failures across the five 30 MHz bands used in this survey. The results show that the lower-frequency band (72–103 MHz) is significantly more susceptible to failure, particularly during imaging.

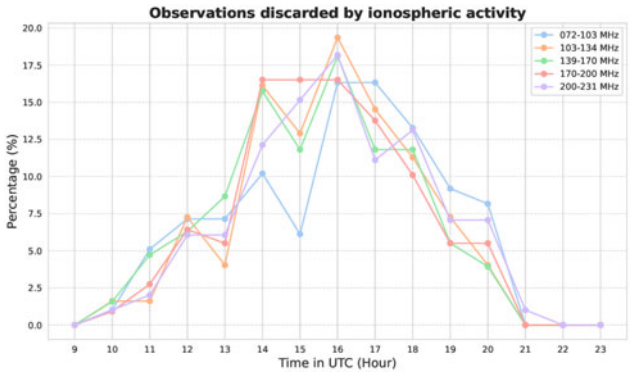


Figure A1. Distribution of the observations discarded across the five 30 MHz frequency channels due to strong ionospheric activity.

These increased losses are primarily attributed to enhanced RFI contamination and ionospheric turbulence.

To quantify the impact of ionospheric activity, Figure A1 presents the fraction of observations discarded as a function of time, clearly illustrating periods of increased data loss across all five frequency channels, probably caused by ionospheric disturbances.

Appendix B. Noise levels

The RMS noise across the GLEAM-X: GP region is shown in Figure B1. Noise levels generally increase toward the Galactic centre and at northern hemisphere longitudes. Peaks observed across the five frequency bands are primarily caused by the presence of sources; for example, the peak near longitude 325° corresponds to a cluster. An exception is the 200–231 MHz band, where the peaks are also influenced by reduced mosaic quality, which results from a smaller field of view at higher frequencies, leading to less coverage during the mosaicking process compared to lower channels. However, this trend does not significantly affect the wideband image, which maintains values < 10 mJy beam^{-1} across most of the longitude range.

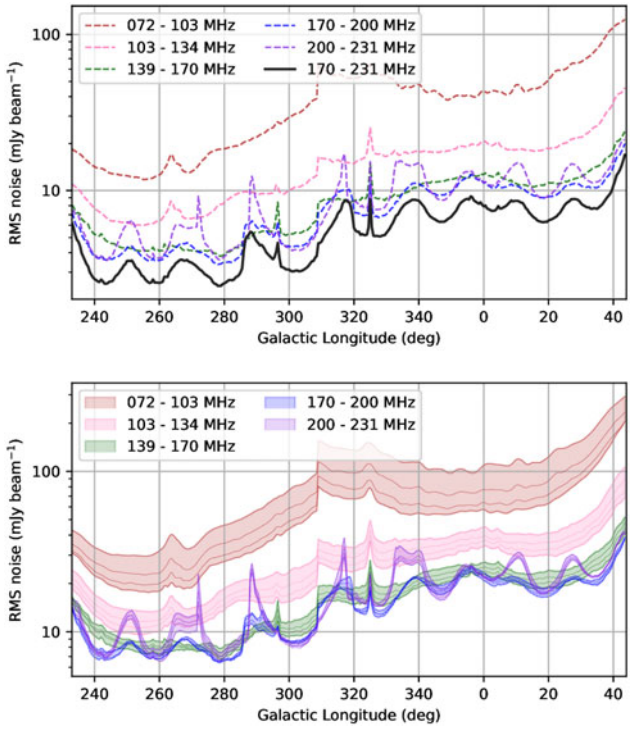


Figure B1. Variation of RMS noise across the GLEAM-X: GP longitude range. Top panel: RMS trends for the five 30 MHz bands (dashed lines) and the wideband image. Bottom panel: RMS trends for the 20×7.68 MHz sub-bands. Shaded regions indicate the frequency ranges corresponding to the four bands that make up the broader images.

Appendix C. (*u*, *v*) coverage

A visualisation of the instrument Phase I and Phase II (u, v)-coverage is reported in Figure C1. The dense core of the MWA Phase I configuration is key for detecting the larger structures of the Galaxy. In the 'extended' Phase ii configuration, the abundance of short baselines has been reduced, and hence dropping sharply the sensitivity above $\approx 20'$; the longest baseline, instead, has been doubled in order to gain sensitivity to the finest scales.

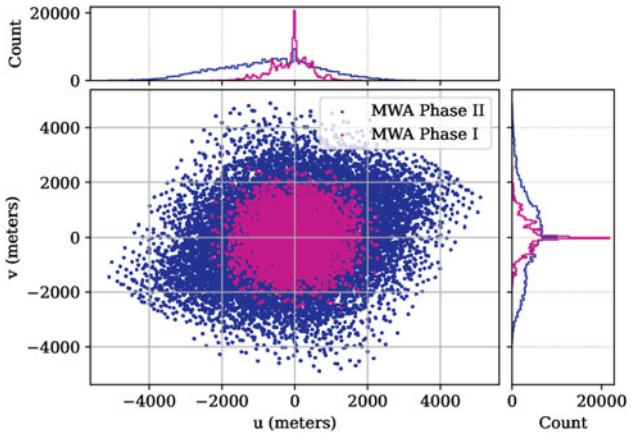


Figure C1. (u, v)-coverage for the MWA Phase i (blue) and Phase ii (red) configurations.

https://doi.org/10.1017/pasa.2025.10094 Published online by Cambridge University Press

Appendix D. Observations employed

The successful 1 898 observations used in this work are compiled in a CSV table. For each observation, we provide the central frequency, start time, coordinates (in both FK5 and Galactic systems), and pointing information (elevation and azimuth). Observations are grouped by frequency channel and ordered sequentially in time. The initial four entries are presented in Table D1.

Table D1. Example of a summary table comprising the list of GLEAM and GLEAM-X observations used to create the final mosaic of the GP for channel 72–103 MHz. A table is generated for all five frequency channels. The table includes the observation ID, the central frequency, the time the observation started, the Azimuth (Az) and Elevation (El) of the pointing, the RA and Dec coordinates in degrees, and the l and b coordinates in degrees.

Observation ID	Freq. (MHz)	Start time (UTC)	Az(°)	El(°)	RA(°)	Dec(°)	l(°)	b(°)
1079096624	87.68	2014-03-17 13:43:28	180.0	61.7	137.5	−54.9	274.6	−4.8
1102969536	87.68	2014-12-18 20:25:20	194.0	60.7	138.4	−54.6	274.7	−4.1
1204209616	87.68	2018-03-04 14:39:58	180.0	61.7	138.8	−54.9	275.1	−4.2
1204982096	87.68	2018-03-13 13:14:38	166.0	60.7	138.1	−54.6	274.6	−4.2

https://doi.org/10.1017/pasa.2025.10094 Published online by Cambridge University Press